Ab initio derivation of electronic low-energy models for C_{60} and aromatic compounds

Yusuke Nomura,[1] Kazuma Nakamura,[1,2] and Ryotaro Arita[1,2,3]

[1]*Department of Applied Physics, University of Tokyo, 7-3-1 Hongo, Bunkyo-ku, Tokyo JP-113-8656, Japan*

[2]*JST CREST, 7-3-1 Hongo, Bunkyo-ku, Tokyo JP-113-8656, Japan*

[3]*JST PRESTO, Kawaguchi, Saitama JP-332-0012, Japan*

(Received 7 December 2011; revised manuscript received 26 February 2012; published 25 April 2012)

We present a systematic study for understanding the relation between electronic correlation and superconductivity in C_{60} and aromatic compounds. We derived, from first principles, extended Hubbard models for twelve compounds: fcc K_3C_{60}, Rb_3C_{60}, Cs_3C_{60} (with three different lattice constants), A15 Cs_3C_{60} (with four different lattice constants), doped solid picene, coronene, and phenanthrene. We show that these compounds are strongly correlated and have similar energy scales of their bandwidths and interaction parameters. However, they have a different trend in the relation between the strength of the electronic correlation and superconducting-transition temperature. While the C_{60} compounds have a positive correlation, the aromatic compounds exhibit a negative correlation.

DOI: 10.1103/PhysRevB.85.155452 PACS number(s): 74.20.Pq, 74.70.Kn, 74.70.Wz

I. INTRODUCTION

Superconductivity in π-electron systems, the history of which dates back to studies on graphite-intercalation compounds in the 1960s,[1] has attracted broad interest in condensed-matter physics. Recently, two seminal discoveries for carbon-based superconductors have been reported. One is A15 and/or fcc Cs_3C_{60}, based on a new method to synthesize highly crystalline samples.[2–6] The observed superconducting-transition temperatures (T_c) for the high-pressure samples are found to be as high as 38 K for the A15 and 35 K for the fcc compounds. The other is potassium-doped solid picene,[7] which opened a new avenue to various *aromatic superconductors* for which the maximum T_c has reached 33 K.[8–11]

The mechanism of superconductivity of these new superconductors has not been fully understood. For alkali-doped fullerides, while there are several experimental reports which seemingly support the conventional Bardeen-Cooper-Schrieffer (BCS) mechanism, various indications for unconventional superconductivity have been also observed. For example, although the positive correlation between T_c and the lattice constant found in K- and Rb-doped fullerides has been understood in terms of the standard BCS theory,[12] more recent experiments for larger cations have revealed that T_c does not necessarily behave monotonically as a function of the lattice parameters.[2–6] The fact that the superconducting phase has a domelike shape in the phase diagram is indeed reminiscent of cuprates[13] and unconventional organic superconductors such as bis(ethylenedithio)-tetrathiafulvalene (BEDT-TTF).[14] In addition, these new C_{60} superconductors are insulators at ambient pressure,[2–6] indicating that the superconducting phase resides in the vicinity of an insulating phase. In fact, considering these characteristic features, it has been proposed that the interplay between the orbital, spin, and lattice degrees of freedom is the origin of the high-T_c superconductivity.[15]

For aromatic superconductors, following the discovery of K-doped picene ($C_{22}H_{14}$),[7] it has been found that various hydrocarbon compounds such as coronene ($C_{24}H_{12}$), phenanthrene ($C_{14}H_{10}$), and 1,2:8,9-dibenzopentacene ($C_{30}H_{18}$) also exhibit superconductivity.[8–11] The diversity of hydrocarbon molecules suggests the possibility of new and higher-T_c aromatic superconductors. So far, the electronic structure,[16–20] electronic correlations,[21,22] electron-phonon interactions,[23,24] exiton and plasmon properties of the normal state[25–28] have been studied while studies on superconducting properties are still limited. The pairing mechanism is totally an open question.[29]

There are several similarities between C_{60} and aromatic superconductors; they are both molecular solids having narrow bands around the Fermi level, whose energy scales compete with those of the electron-phonon and electron-electron interactions. The competition among these three factors is a characteristic aspect of carbon-based materials. *Ab initio* derivations of effective low-energy models for these compounds are important to make the situation transparent and to clarify the origin of their high-T_c superconductivity. By comparing the parameters in the effective models for the C_{60} and aromatic superconductors, the differences and similarities are quantitatively identified and analyzed.

Recent methodology for the construction of the electronic model, based on the combination use of the maximally localized Wannier orbital (MLWO) (Ref. 30) and the constrained-random-phase approximation (cRPA),[31] extends its applicability range. It does not place limitations on the character of basis orbitals of the effective model whether atomic or molecular. Indeed, it has already been applied to various complex systems such as BEDT-TTF (Refs. 32 and 33) and zeolites.[34] While electronic-interaction parameters of the C_{60} and aromatic superconductors have been estimated by various methods,[26,35–38] explicit and direct comparison of these systems by the same method has yet to be done. Thus, it is imperative to evaluate the interaction parameters of C_{60} and aromatic superconductors by exploiting the state-of-the-art technique and perform a systematic comparison. In the present study, we constructed *ab initio* extended Hubbard models which describe the low-energy electronic structures of twelve examples of C_{60} and aromatic compounds. The transfer integrals were given as matrix elements of the Kohn-Sham Hamiltonian in the Wannier basis. The interaction parameters were evaluated by calculating the Wannier-matrix elements of the screened Coulomb interaction, which is obtained by

cRPA. The estimated correlation strength as the ratio of the interaction energy to the kinetic one is nearly at or beyond unity for the studied materials, indicating that both the C_{60} and aromatic systems are classified as strongly correlated electron systems. On the other hand, we observed a notable difference between the two systems; for the C_{60} system, there exists a positive-correlation regime in the correlation strength and the experimental T_c. In contrast, the aromatic system exhibits negative correlation between these two quantities.

This paper is organized as follows. In Sec. II, we show how to construct the low-energy models from *ab initio* calculations. In Sec. III, we show the calculated band structure, MLWOs, transfer integrals, and effective interaction parameters. We discuss the material dependence of the derived parameters and relation between the strength of the electronic correlation and superconductivity in Sec. IV. Finally, we give a summary in Sec. V.

II. METHODS

We derive electronic low-energy models with the combination of MLWOs and the cRPA. This method has widely been applied to the derivation of effective models for $3d$ transition metals,[39,40] their oxides,[39] organic conductors,[32,33] zeolites,[34] iron-based superconductors,[41,42] and $5d$-transition-metal oxides.[43] We first perform band calculations based on density functional theory (DFT)[44,45] and choose "target bands" of the effective model. By constructing MLWOs for the target bands, we calculate transfer integrals and effective interactions in the effective model. In the calculation of the effective interaction, the screening by electrons besides target-band electrons is considered within the cRPA (see below).

We apply this scheme to the derivation of effective models, i.e., extended multiorbital Hubbard models, for the C_{60} and aromatic compounds. The Hamiltonian consists of the transfer part $\mathcal{H}_t$, the Coulomb-repulsion part $\mathcal{H}_U$, and the exchange-interactions and pair-hopping part $\mathcal{H}_J$ defined as

$$\mathcal{H} = \mathcal{H}_t + \mathcal{H}_U + \mathcal{H}_J, \tag{1}$$

where

$$\mathcal{H}_t = \sum_{\sigma} \sum_{ij} \sum_{nm} t_{nm}(\mathbf{R}_{ij}) a_{in}^{\sigma\dagger} a_{jm}^{\sigma}, \tag{2}$$

$$\mathcal{H}_U = \frac{1}{2} \sum_{\sigma\rho} \sum_{ij} \sum_{nm} U_{nm}(\mathbf{R}_{ij}) a_{in}^{\sigma\dagger} a_{jm}^{\rho\dagger} a_{jm}^{\rho} a_{in}^{\sigma}, \tag{3}$$

$$\mathcal{H}_J = \frac{1}{2} \sum_{\sigma\rho} \sum_{ij} \sum_{nm} J_{nm}(\mathbf{R}_{ij}) \times \left(a_{in}^{\sigma\dagger} a_{jm}^{\rho\dagger} a_{in}^{\rho} a_{jm}^{\sigma} + a_{in}^{\sigma\dagger} a_{in}^{\rho\dagger} a_{jm}^{\rho} a_{jm}^{\sigma} \right), \tag{4}$$

with $a_{in}^{\sigma\dagger}$ (a_{in}^{σ}) being a creation (annihilation) operator of an electron with spin σ in the nth MLWO localized at a C_{60}- or aromatic-hydrocarbon molecule located at $\mathbf{R}_i$ and where $\mathbf{R}_{ij} = \mathbf{R}_i - \mathbf{R}_j$. The parameters $t_{nm}(\mathbf{R}_{ij})$ represent an on-site energy ($\mathbf{R}_{ij} = \mathbf{0}$) and hopping integrals ($\mathbf{R}_{ij} \neq \mathbf{0}$), which are described with the translational symmetry as

$$t_{nm}(\mathbf{R}) = \langle \phi_{n\mathbf{R}} | \mathcal{H}_{\mathrm{KS}} | \phi_{m\mathbf{0}} \rangle, \tag{5}$$

where $|\phi_{n\mathbf{R}_i}\rangle = a_{in}^{\dagger}|0\rangle$ and $\mathcal{H}_{\mathrm{KS}}$ is the Kohn-Sham Hamiltonian.[46]

To evaluate effective interaction parameters $U_{nm}(\mathbf{R})$ and $J_{nm}(\mathbf{R})$, we calculate the screened Coulomb interaction $W(\mathbf{r},\mathbf{r}')$ at the low-frequency limit. We first calculate the noninteracting-polarization function χ, excluding polarization processes within the target bands. Note that screening by the target electrons is considered when we solve the effective models so that we have to avoid double counting of it when we derive the effective models. With the resulting χ, the W interaction is calculated as $W = (1 - v\chi)^{-1}v$, where v is the bare Coulomb interaction $v(\mathbf{r},\mathbf{r}') = \frac{1}{|\mathbf{r}-\mathbf{r}'|}$.

Once the screened Coulomb interaction $W(\mathbf{r},\mathbf{r}')$ is calculated, the matrix elements of W are obtained as

$$\begin{aligned} U_{nm}(\mathbf{R}) &= \langle \phi_{n\mathbf{R}} \phi_{m\mathbf{0}} | W | \phi_{n\mathbf{R}} \phi_{m\mathbf{0}} \rangle \\ &= \int\int d\mathbf{r} d\mathbf{r}' \phi_{n\mathbf{R}}^{*}(\mathbf{r}) \phi_{n\mathbf{R}}(\mathbf{r}) W(\mathbf{r},\mathbf{r}') \phi_{m\mathbf{0}}^{*}(\mathbf{r}') \phi_{m\mathbf{0}}(\mathbf{r}') \end{aligned} \tag{6}$$

and

$$\begin{aligned} J_{nm}(\mathbf{R}) &= \langle \phi_{n\mathbf{R}} \phi_{m\mathbf{0}} | W | \phi_{m\mathbf{0}} \phi_{n\mathbf{R}} \rangle \\ &= \int\int d\mathbf{r} d\mathbf{r}' \phi_{n\mathbf{R}}^{*}(\mathbf{r}) \phi_{m\mathbf{0}}(\mathbf{r}) W(\mathbf{r},\mathbf{r}') \phi_{m\mathbf{0}}^{*}(\mathbf{r}') \phi_{n\mathbf{R}}(\mathbf{r}'). \end{aligned} \tag{7}$$

For comparison with the cRPA results, we calculate interaction parameters with different levels of screening. One is the unscreened one, i.e., the bare Coulomb interaction, and the other is the fully screened one wherein we calculate χ, including the target-band screening. To distinguish these from the cRPA, we denote them as "bare" and "fRPA" (fully screened random-phase approximation).

III. RESULTS

A. Calculation conditions

We performed DFT band calculations with the TOKYO AB INITIO PROGRAM PACKAGE,[47] based on the pseudopotential-plus-plane-wave framework. We used the generalized-gradient approximation (GGA) exchange-correlation functional with the parametrization of Perdew-Burke-Ernzerhof[48] and Troullier-Martins norm-conserving pseudopotentials[49] in the Kleinman-Bylander representation.[50] The pseudopotentials for alkali metals, K, Rb, and Cs, were supplemented with partial core correction.[51] The cutoff energies for wave functions and charge densities were set to 36 Ry and 144 Ry, respectively, and we employed $5 \times 5 \times 5$ k-point sampling. We confirmed that this condition ensures well converged results.

The DFT calculations were performed for the following twelve materials: fcc K_3C_{60}, fcc Rb_3C_{60}, fcc Cs_3C_{60} with three different lattice parameters, A15 Cs_3C_{60} with four different lattice parameters, doped solid picene, coronene, and phenanthrene. The lattice parameters were taken from the experiments, and internal coordinates were optimized.[53] In fcc A_3C_{60}, the disorder of the orientation of C_{60} molecules was ignored, so the crystal symmetry is lowered from $Fm\bar{3}m$ to $Fm\bar{3}$.

Before presenting the computational results, we summarize the basic properties of the compounds studied in the present paper. Table I lists experimental values for the C_{60}

TABLE I. Basic properties of fcc and A15 alkali-doped C_{60} compounds: the lattice parameter a, corresponding C_{60}^{3-} volume in the solid, and measured superconducting-transition temperature T_c or the Néel temperature T_N. For fcc Cs_3C_{60}, the three samples are specified with the C_{60}^{3-} volume and correspond to those in the superconducting phases with maximum T_c ($V_{SC}^{opt\text{-}P}$), in the vicinity of the metal-insulator transition (V_{MIT}), and in the antiferromagnetic-insulating phase (V_{AFI}), respectively. For the A15 structure, we also list another sample with a higher pressure for which T_c is lower than that of $V_{SC}^{opt\text{-}P}$ and is abbreviated to $V_{SC}^{high\text{-}P}$.

Compound	a (Å)	Volume/C_{60}^{3-} (Å^3)	Pressure (kbar)	T_c (T_N) (K)	Ref.
fcc-K	14.240	722	0	19	52
fcc-Rb	14.420	750	0	29	52
fcc-Cs($V_{SC}^{opt\text{-}P}$)	14.500	762	7	35	4
fcc-Cs(V_{MIT})	14.640	784	2	26	4
fcc-Cs(V_{AFI})	14.762	804	0	(2.2)	4
A15-Cs($V_{SC}^{high\text{-}P}$)	11.450	751	15	35	3
A15-Cs($V_{SC}^{opt\text{-}P}$)	11.570	774	7	38	3
A15-Cs(V_{MIT})	11.650	791	3	32	3
A15-Cs(V_{AFI})	11.783	818	0	(46)	3

compounds, including the lattice constant a, the volume per C_{60}^{3-} in the solid,[57] the applied pressure, and the measured superconducting-transition temperature T_c or the Néel temperature T_N. The a value and/or C_{60}^{3-} volume can be controlled by the chemical and external pressures. In this table, the samples are arranged in the order of increasing lattice constants. For fcc A_3C_{60}, T_c first increases and reaches its maximum (35 K) around $a = 14.500$ Å. Then, it decreases to $T_c \sim 25$ K where the system experiences the metal-insulator transition (MIT) and becomes an antiferromagnetic insulator (AFI) for which the Néel temperature T_N is around 2.2 K. A similar behavior is observed in the A15 system while T_N is significantly higher (46 K). This is because the A15 structure is bipartite and therefore less frustrated.[58] Hereafter, we label the nine C_{60} compounds as fcc-K, fcc-Rb, fcc-Cs($V_{SC}^{opt\text{-}P}$), fcc-Cs(V_{MIT}), fcc-Cs(V_{AFI}), A15-Cs($V_{SC}^{high\text{-}P}$), A15-Cs($V_{SC}^{opt\text{-}P}$), A15-Cs(V_{MIT}), and A15-Cs(V_{AFI}).

Table II shows the experimental lattice parameters for undoped solid picene, coronene, and phenanthrene and the T_c values observed for the doped systems. For doped solid picene, two different T_c values (18 K and 7 K) have been observed depending on the preparation conditions.[7] The superconductivity appears when the system is doped, but the details of the crystal structures in the superconducting phases have not been determined. Thus in the present study, the band calculations for aromatic compounds were performed for the artificially charged system for which three negative charges per one hydrocarbon molecule were doped with a uniform, compensating, positive background charge. For geometries, we employed the experimental ones listed in Table II. Hereafter, doped solid picene, coronene, and phenanthrene are referred to as solid picene^{3-}, coronene^{3-}, and phenanthrene^{3-}, respectively.

TABLE II. Lattice parameters for pristine solid picene, coronene, and phenanthrene and the superconducting-transition temperatures T_c observed for their doped systems.

Compound	a (Å)	b (Å)	c (Å)	β (°)	T_c (K)	Refs.
picene	8.480	6.154	13.515	90.46	18,7	7,54
coronene	16.094	4.690	10.049	110.79	15	10,55
phenanthrene	8.453	6.175	9.477	98.28	5–6	8,9

B. Band structure and density of states

Figure 1 shows our calculated GGA band structures for the fcc A_3C_{60} (upper five panels), A15 Cs_3C_{60} (middle four panels), and aromatic compounds (lower three panels). These compounds have common features in their band structures; i.e., we see narrow bands near the Fermi level separated from other bands, being preferable when we choose the target bands to construct an effective model. In the C_{60} compounds, there are threefold-degenerate states, which form the so-called "t_{1u} band" near the Fermi level, and we construct effective models for these bands. For aromatic compounds, the target bands are made from the two lowest unoccupied molecular orbitals (LUMO and LUMO+1) in an isolated molecule.[16,19,20] It should be noted that unoccupied bands lie above the target bands more densely in the order of solid picene^{3-}, solid coronene^{3-}, and solid phenanthrene^{3-}. Since conduction bands can generate stronger screening when they reside closer to the target bands, we expect a weak repulsive interaction in solid picene^{3-} compared to the other two.

We show in Fig. 2 the calculated density of states (DOS) of the t_{1u} band for fcc A_3C_{60} [Fig. 2(a)] and A15 Cs_3C_{60} [Fig. 2(b)]. For both fcc and A15 compounds, the bandwidth W monotonically increases as the lattice constant decreases, but the DOS profile does not change drastically. We list the values of W in Table III. The bandwidth of the A15 compound ($\sim$0.6 eV) tends to be larger than that of the fcc compound ($\sim$0.4 eV), which is due to the difference in the inter-C_{60} contact, i.e., the "hexagon-to-hexagon" configuration for the A15 and "bond-to-bond" one for the fcc compound.[59] It was found that the bandwidths of the aromatic compounds are nearly 0.5 eV (see Table III).

C. Maximally localized Wannier orbitals

Figure 3 shows a contour plot of one of the MLWOs for the t_{1u} bands of A15-Cs(V_{AFI}). The results of other C_{60} compounds are almost the same. From this figure we see that the resulting Wannier orbital is well localized at the single C_{60} molecule. In this plot, we displayed the same orbital along the three directions; Figs. 3(a), 3(b), and 3(c) correspond to the views along the x, y, and z axes, respectively. We see a node in the center of this orbital for Figs. 3(b) and 3(c); thus, this orbital has p_x-like symmetry. Note that the view along the y axis is not identical to the view along the z axis, which is in contrast with the case of atomic p orbitals. We note that the other two p_y- and p_z-like Wannier orbitals are symmetrically equivalent to the presented p_x-like orbital. We also note that the weight of the Wannier orbitals concentrates in the vicinity of the cage of the C_{60} molecule and that there is little weight inside it.

We next show in Fig. 4 a contour plot of two MLWOs of solid phenanthrene^{3-}. In the aromatic compounds, the two

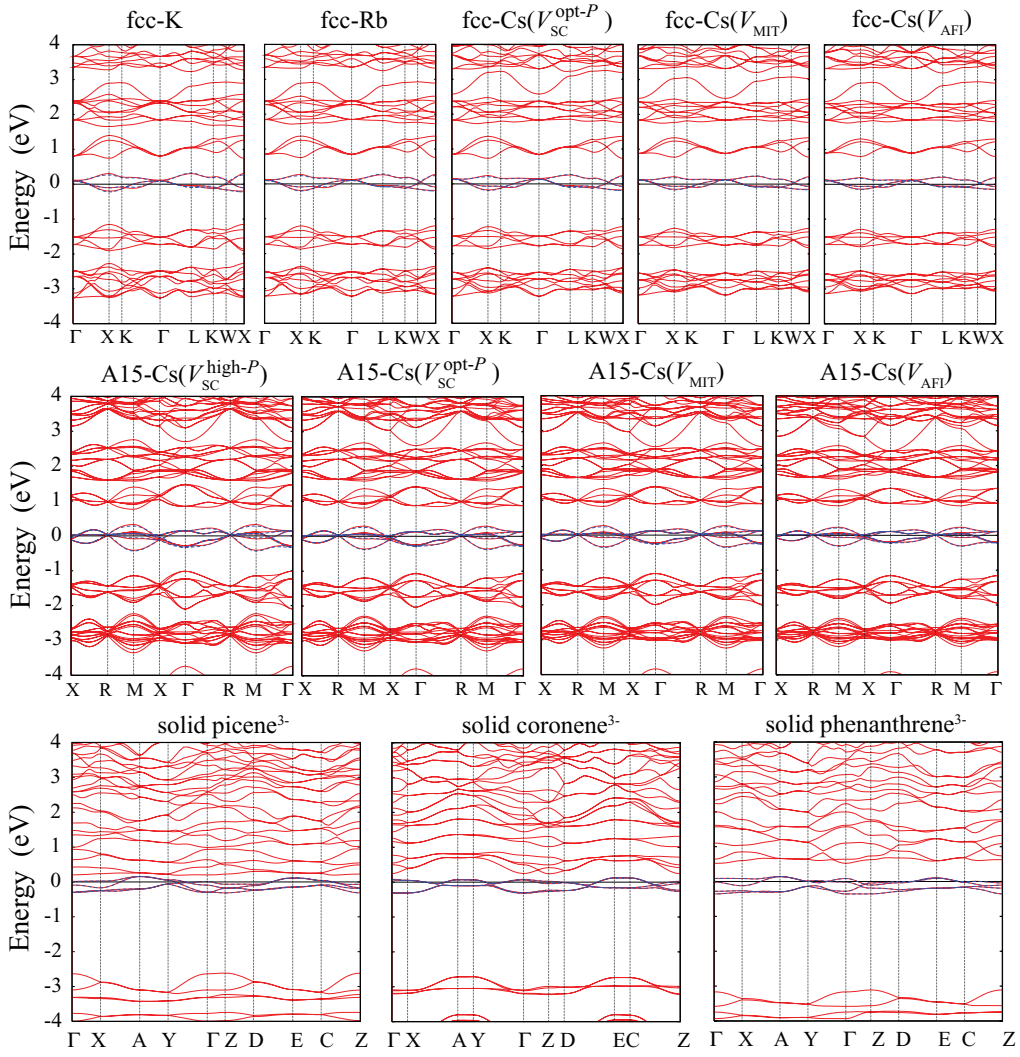

FIG. 1. (Color online) Calculated *ab initio* electronic band structure of fcc-K, fcc-Rb, fcc-Cs($V_{SC}^{opt\text{-}P}$), fcc-Cs(V_{MIT}), fcc-Cs(V_{AFI}), A15-Cs($V_{SC}^{opt\text{-}P}$), A15-Cs($V_{SC}^{high\text{-}P}$), A15-Cs(V_{MIT}), A15-Cs(V_{AFI}), solid picene^{3-}, solid coronene^{3-}, and solid phenanthrene^{3-}. In the case of aromatic compounds with monoclinic structures, the horizontal axis is labeled by the special points in the Brillouin zone with Γ, X, A, Y, Z, D, E, and C, respectively, corresponding to (0, 0, 0), (1/2, 0, 0), (1/2, 1/2, 0), (0, 1/2, 0), (0, 0, 1/2), (1/2, 0, 1/2), (1/2, 1/2, 1/2), and (0, 1/2, 1/2), respectively, in units of ($\boldsymbol{a}^*$,$\boldsymbol{b}^*$,$\boldsymbol{c}^*$). The interpolated-band dispersion with the derived tight-binding Hamiltonian is depicted as blue dashed lines.

basis orbitals of the effective model are not symmetrically equivalent, and therefore, we specify these orbitals as "lower" and "higher" orbitals in terms of the on-site level of the MLWOs. The lower and higher orbitals are shown in Figs. 4(a) and 4(b), respectively. We again see the resulting orbitals are well localized at the single molecules. The MLWOs of solid picene^{3-} and coronene^{3-} are similar to those of undoped systems calculated in Refs. 16 and 20.

TABLE III. Calculated bandwidth W of the target band and spatial Wannier spread Ω for twelve materials: fcc-K, fcc-Rb, fcc-Cs($V_{SC}^{opt\text{-}P}$), fcc-Cs(V_{MIT}), fcc-Cs(V_{AFI}), A15-Cs($V_{SC}^{high\text{-}P}$), A15-Cs($V_{SC}^{opt\text{-}P}$), A15-Cs(V_{MIT}), A15-Cs(V_{AFI}), solid picene^{3-}, solid coronene^{3-}, and solid phenanthrene^{3-}. For the aromatic compounds, the two values of Ω are listed; the left is the "lower-level" orbital, and the right is the "higher-level" one. Units are given in meV for W and Å for Ω.

	fcc A_3C_{60}					A15 Cs_3C_{60}				Aromatic compounds		
	K	Rb	Cs($V_{SC}^{opt\text{-}P}$)	Cs(V_{MIT})	Cs(V_{AFI})	$V_{SC}^{high\text{-}P}$	$V_{SC}^{opt\text{-}P}$	V_{MIT}	V_{AFI}	picene^{3-}	coronene^{3-}	phenanthrene^{3-}
W	502	454	427	379	341	740	659	614	535	477	447	505
Ω	4.28	4.21	4.19	4.14	4.10	4.27	4.20	4.16	4.12	4.08, 4.13	3.64, 3.67	3.20, 3.08

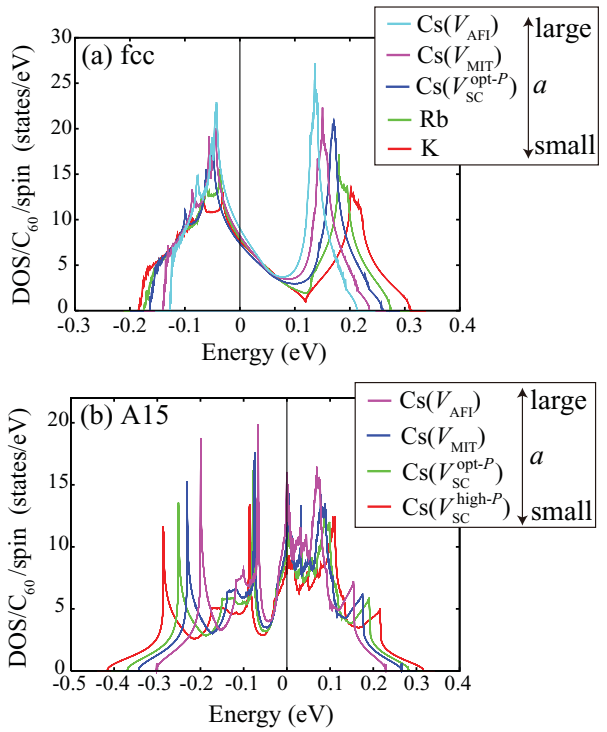

FIG. 2. (Color online) (a) Our calculated density of states (DOS) for the t_{1u} band of fcc-K (red), fcc-Rb (green), fcc-Cs($V_{SC}^{opt\text{-}P}$) (blue), fcc-Cs(V_{MIT}) (purple), and fcc-Cs(V_{AFI}) (light blue). (b) DOS for the t_{1u} band of A15-Cs($V_{SC}^{high\text{-}P}$) (red), A15-Cs($V_{SC}^{opt\text{-}P}$) (green), A15-Cs(V_{MIT}) (blue), and A15-Cs(V_{AFI}) (purple).

We list in Table III our calculated spatial spread Ω_n of the MLWOs for the 12 materials wherein Ω_n is defined as

$$\Omega_n = \sqrt{\langle\phi_{n\mathbf{0}}|r^2|\phi_{n\mathbf{0}}\rangle - |\langle\phi_{n\mathbf{0}}|\mathbf{r}|\phi_{n\mathbf{0}}\rangle|^2}. \quad (8)$$

In the C_{60} compounds, the calculated Wannier spread is roughly 4 Å, and thus, the estimated effective volume $\frac{4}{3}\pi\Omega^3$ is $\sim$268 Å^3. The value is compared with the $C_{60}{}^{3-}$ volume listed in Table I ($\sim$720–820 Å^3), clearly indicating the well-localized nature of the MLWO on the single molecule. We see that the Wannier spread has a weak positive correlation with the bandwidth W. In the aromatic compounds, the molecular sizes themselves are different from each other, resulting in the appreciable difference in Ω values. Note that Ω has no clear correlation with W.

D. Transfer integrals

Let us move on to transfer integrals. For the C_{60} compounds, the band dispersion of the target band was found to be well reproduced only with nearest-neighbor (NN) and next-nearest-neighbor (NNN) transfers. The orbital indices 1, 2, and 3 denote p_x-, p_y-, and p_z-like orbitals, respectively. On-site energies for the three MLWOs are set to zero. From now on, "site" means one molecule, and the coordinate of site $\mathbf{R}$ is defined as the center of the molecule. The transfer integrals $t_{nm}(\mathbf{R})$ are represented as 3×3 matrices. In the fcc (A15) structure, there are 12 (8) NN sites and 6 (6) NNN sites per molecule. From transfers to the specific site, other transfers to the equivalent sites are reproduced by proper

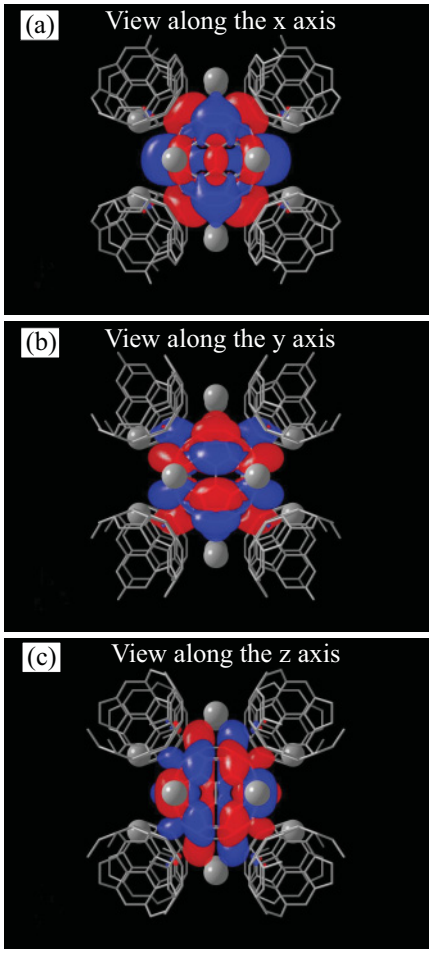

FIG. 3. (Color online) Isosurfaces of our calculated p_x-like maximally localized Wannier orbital of A15-Cs(V_{AFI}) viewed along the (a) x axis, (b) y axis, (c) z axis, drawn by VESTA (Ref. 60). The red surfaces indicate positive isosurfaces, and the blue surfaces indicate negative isosurfaces.

symmetry operations. As a representative NN site, we choose $\mathbf{R} = (R_x, R_y, R_z) = (0.5,0.5,0.0)$ and $(0.5,0.5,0.5)$ for the fcc and A15 structures, respectively, where the coordinate is based on the conventional cell. The transfer matrices to these sites are

$$\begin{pmatrix} F_1 & F_2 & 0 \\ F_2 & F_3 & 0 \\ 0 & 0 & F_4 \end{pmatrix} \quad \text{and} \quad \begin{pmatrix} A_1 & A_{2(3)} & A_{3(2)} \\ A_{3(2)} & A_1 & A_{2(3)} \\ A_{2(3)} & A_{3(2)} & A_1 \end{pmatrix} \quad (9)$$

for the fcc and A15 structures, respectively. In the A15 structure, the two C_{60} molecules in the unit cell (denoted as the A- and B-sites) are not equivalent in terms of their orientations. So in the matrix in Eq. (9), we show both the transfers from the A-site to the B-site and from the B-site to the A-site (in parentheses). We choose $\mathbf{R} = (1,0,0)$ for a representative NNN site for both structures, and then the transfer matrices are written as

$$\begin{pmatrix} F_5 & 0 & 0 \\ 0 & F_6 & 0 \\ 0 & 0 & F_7 \end{pmatrix} \quad \text{and} \quad \begin{pmatrix} A_4 & 0 & 0 \\ 0 & A_{5(6)} & 0 \\ 0 & 0 & A_{6(5)} \end{pmatrix} \quad (10)$$

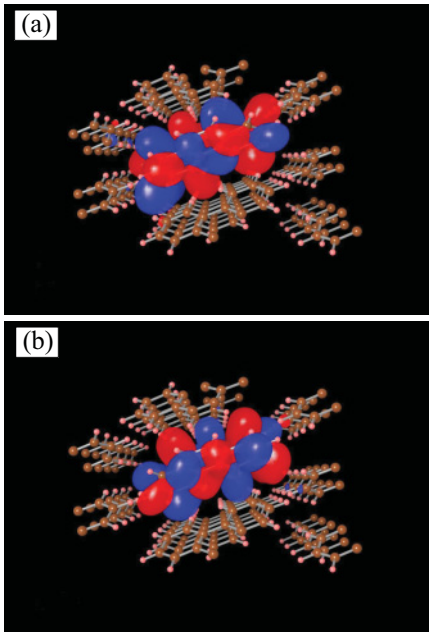

FIG. 4. (Color online) Isosurfaces of maximally localized Wannier orbitals of solid phenanthrene^{3-} with (a) lower on-site energy and (b) higher on-site energy, drawn by VESTA (Ref. 60). The red surfaces indicate positive isosurfaces, and the blue surfaces indicate negative isosurfaces.

for the fcc and A15 structures, respectively. The transfer matrix for the A15 structure represents the A-A transfer, and the B-B one is in parentheses. Table IV shows the value of the parameters from F_1 to F_7 for the fcc C_{60} compounds. We note that $F_6 \neq F_7$ is due to the lowering of the symmetry from $Fm\bar{3}m$ to $Fm\bar{3}$. Table V shows the values of parameters from A_1 to A_6 for A15 Cs_3C_{60}. For both systems, the values of the hopping parameters decrease as those of the lattice parameters increase.

We next describe the procedure for obtaining transfers to the other NN sites or NNN sites. First, we consider the NN case. For the fcc structure, the transfer matrices to the other five NN sites are written with F_1–F_4 as follows:

$$\begin{pmatrix} F_4 & 0 & 0 \\ 0 & F_1 & F_2 \\ 0 & F_2 & F_3 \end{pmatrix} \quad \text{for} \quad \mathbf{R} = (0.0,0.5,0.5),$$

$$\begin{pmatrix} F_4 & 0 & 0 \\ 0 & F_1 & -F_2 \\ 0 & -F_2 & F_3 \end{pmatrix} \quad \text{for} \quad \mathbf{R} = (0.0,0.5,-0.5),$$

TABLE IV. Hopping parameters for fcc A_3C_{60} in Eqs. (9) and (10). Units are given in 10^{-4} eV.

Compound	F_1	F_2	F_3	F_4	F_5	F_6	F_7
fcc-K	−40	−339	421	−187	−94	−14	−2
fcc-Rb	−16	−306	392	−159	−75	−8	15
fcc-Cs($V_{\rm SC}^{\text{opt-}P}$)	26	−299	372	−120	−60	−3	36
fcc-Cs($V_{\rm MIT}$)	15	−267	332	−104	−40	1	30
fcc-Cs($V_{\rm AFI}$)	13	−241	302	−94	−33	1	24

TABLE V. Hopping parameters for A15 Cs_3C_{60} in Eqs. (9) and (10). Units are given in 10^{-4} eV.

Compound	A_1	A_2	A_3	A_4	A_5	A_6
A15-Cs($V_{\rm SC}^{\text{high-}P}$)	−297	448	67	74	−105	−289
A15-Cs($V_{\rm SC}^{\text{opt-}P}$)	−262	400	61	74	−97	−239
A15-Cs($V_{\rm MIT}$)	−239	371	57	76	−89	−212
A15-Cs($V_{\rm AFI}$)	−206	329	53	73	−79	−180

$$\begin{pmatrix} F_3 & 0 & F_2 \\ 0 & F_4 & 0 \\ F_2 & 0 & F_1 \end{pmatrix} \quad \text{for} \quad \mathbf{R} = (0.5,0.0,0.5),$$

$$\begin{pmatrix} F_3 & 0 & -F_2 \\ 0 & F_4 & 0 \\ -F_2 & 0 & F_1 \end{pmatrix} \quad \text{for} \quad \mathbf{R} = (-0.5,0.0,0.5),$$

$$\begin{pmatrix} F_1 & -F_2 & 0 \\ -F_2 & F_3 & 0 \\ 0 & 0 & F_4 \end{pmatrix} \quad \text{for} \quad \mathbf{R} = (0.5,-0.5,0.0).$$

For the A15 structure, we have

$$\begin{pmatrix} A_1 & A_{2(3)} & -A_{3(2)} \\ A_{3(2)} & A_1 & -A_{2(3)} \\ -A_{2(3)} & -A_{3(2)} & A_1 \end{pmatrix} \quad \text{for} \quad \mathbf{R} = (0.5,0.5,-0.5),$$

$$\begin{pmatrix} A_1 & -A_{2(3)} & A_{3(2)} \\ -A_{3(2)} & A_1 & -A_{2(3)} \\ A_{2(3)} & -A_{3(2)} & A_1 \end{pmatrix} \quad \text{for} \quad \mathbf{R} = (0.5,-0.5,0.5),$$

$$\begin{pmatrix} A_1 & -A_{2(3)} & -A_{3(2)} \\ -A_{3(2)} & A_1 & A_{2(3)} \\ -A_{2(3)} & A_{3(2)} & A_1 \end{pmatrix} \quad \text{for} \quad \mathbf{R} = (0.5,-0.5,-0.5).$$

The remaining transfers to the NN sites are reproduced by the relation $t_{nm}(\mathbf{R}) = t_{nm}(-\mathbf{R})$.

Similarly, the transfers to the other NNN sites are described as

$$\begin{pmatrix} F_7(A_{6(5)}) & 0 & 0 \\ 0 & F_5(A_4) & 0 \\ 0 & 0 & F_6(A_{5(6)}) \end{pmatrix} \quad \text{for} \quad \mathbf{R} = (0,1,0),$$

$$\begin{pmatrix} F_6(A_{5(6)}) & 0 & 0 \\ 0 & F_7(A_{6(5)}) & 0 \\ 0 & 0 & F_5(A_4) \end{pmatrix} \quad \text{for} \quad \mathbf{R} = (0,0,1),$$

for the fcc (A15) structures, and the remaining NNN transfers are generated according to $t_{nm}(\mathbf{R}) = t_{nm}(-\mathbf{R})$.

Using these NN- and NNN-transfer parameters, we construct the transfer part $\mathcal{H}_t$ in Eq. (2) of the effective model. The band dispersion for the C_{60} compounds calculated from the resulting $\mathcal{H}_t$ is depicted as blue dashed lines in Fig. 1 from which we see that the original GGA band dispersion is satisfactorily reproduced.

For the aromatic compounds, since there is no simple symmetry operation, their transfers are difficult to show concisely.[16,20] For the aromatic compounds, we describe only some characteristic features of the transfers. The aromatic compounds are regarded as the stacking-layered systems, so we expect a two-dimensional hopping structure. However, in the present transfer analysis, we found that the anisotropy

TABLE VI. Comparison between the maximum absolute values of the intralayer transfer $t_\parallel$ and interlayer transfer $t_\perp$ for aromatic compounds. For the three directions in $t_\parallel$, see Fig. 5. Units are given in meV.

Compound	$t_{\parallel 1}^{\max}$	$t_{\parallel 2}^{\max}$	$t_{\parallel 3}^{\max}$	$t_{\perp}^{\max}$
solid picene^{3-}	48	39	59	20
solid coronene^{3-}	7	87	7	14
solid phenanthrene^{3-}	49	32	73	36

of the transfers is not so simple. Table VI compares the maximum absolute values of the intralayer transfers ($t_\parallel$) with those of the interlayer transfers ($t_\perp$) for which the intralayer is defined as the ab plane. The intralayer transfers are further decomposed in the three directions and compared with each other (see Fig. 5 for the definition of the three directions). The anisotropy ($t_\perp^{\max}/t_\parallel^{\max}$) is not so appreciable for solid picene^{3-}, estimated as $20/59 \sim 0.34$, and for phenanthrene^{3-} as $\sim$0.49. In contrast, the anisotropy of coronene^{3-} is significant and is $\sim$0.16. In the case of coronene^{3-}, the intralayer anisotropy is even strong: $t_{\parallel 1}^{\max}/t_{\parallel 2}^{\max} = 7/87 \sim 0.08$; this system is an almost quasi-one-dimensional chain along the b axis. We note that the original GGA band dispersion is well reproduced by short-range-transfer hoppings (Fig. 1).

E. Effective interaction parameters

We performed random-phase-approximation (RPA) calculations to evaluate the screened Coulomb interaction $W(\mathbf{r},\mathbf{r}')$ in Eqs. (6) and (7) in which the dielectric function was expanded in plane waves with an energy cutoff 7.5 Ry for fcc A_3C_{60} and aromatic compounds and 5.0 Ry for A15 Cs_3C_{60}. The total number of bands considered in the polarization function was set to 335 (120 occupied, 3 target, and 212 unoccupied) for fcc A_3C_{60}, 670 (240 occupied, 6 target, and 424 unoccupied) for A15 Cs_3C_{60}, 310 (102 occupied, 4 target, and 204 unoccupied) for solid picene^{3-}, 315 (108 occupied, 4 target, and 203 unoccupied) for solid coronene^{3-}, and 270 (66 occupied, 4 target, and 200 unoccupied) for solid phenanthrene^{3-}. The Brillouin-zone integral on the wave vector was evaluated by the generalized-tetrahedron method.[61] A problem due to the singularity of the long-wavelength-limit Coulomb interaction in the evaluation of the Wannier-matrix elements, $U_{nm}(\mathbf{R})$ in Eq. (6) and $J_{nm}(\mathbf{R})$ in Eq. (7), was treated in the manner described in Ref. 62.

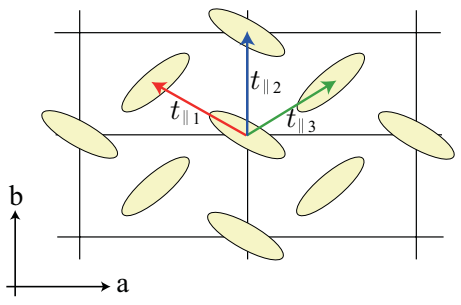

FIG. 5. (Color online) Schematic picture of the intralayer transfer $t_\parallel$ along the three directions in the aromatic compounds. The ellipses indicate molecules.

The on-site interactions are specified by $U = U_{nn}(\mathbf{0})$, $U' = U_{nm}(\mathbf{0})$, and $J = J_{nm}(\mathbf{0})$ for $n \neq m$. In the case of C_{60} compounds, U, U', and J take only one value, according to the symmetry. For aromatic compounds, U is different for two orbitals, so we present two values. We also denote the Coulomb repulsion between the neighboring sites as V.

Table VII shows our calculated interaction parameters U, U', J, and V with three screening levels (bare, cRPA, and fRPA). We see that the value of the Coulomb repulsion decreases as the screening processes increase. In the C_{60} compounds, the bare value is $\sim$3.4 eV, and after considering the screening by cRPA, the value is reduced to $\sim$1 eV. By taking account of the intra-target-band screening by fRPA, the value is further reduced to $\sim$0.1 eV. It should be noted here that the material dependences of the bare values in the fcc and A15 structures are small, for example, 3.27 eV for fcc-K and 3.37 for fcc-Cs($V_{\rm AFI}$). The difference is nearly 3%. This difference is ascribed to the difference in the spatial spread of the MLWOs (see Table III). On the other hand, the material difference in the cRPA values is beyond 20%: 0.82 eV for fcc-K and 1.07 for fcc-Cs($V_{\rm AFI}$). Indeed, this appreciable difference originates from the difference in the macroscopic dielectric constant defined as

$$\epsilon_M^{\rm cRPA} = \lim_{\mathbf{Q}\to 0}\lim_{\omega\to 0}\frac{1}{\epsilon_{\mathbf{GG}}^{\rm cRPA\,-1}(\mathbf{q},\omega)}, \tag{11}$$

with ω being the frequency and $\mathbf{Q} = \mathbf{q} + \mathbf{G}$, where $\mathbf{q}$ is a wave vector in the first Brillouin zone and $\mathbf{G}$ is a reciprocal lattice vector. We list the values at the bottom of the table. We see that the material dependence of $\epsilon_M^{\rm cRPA}$ is appreciable as 5.6 for fcc-K and 4.4 for fcc-Cs($V_{\rm AFI}$), clearly indicating the importance of the screening effect in addition to the spatial Wannier spread.

For the aromatic compounds, differences in both the bare interaction and the screening effect contribute to the material dependence of the cRPA values. The bare interactions are $U_{\rm bare}^{\rm picene^{3-}} \sim U_{\rm bare}^{\rm coronene^{3-}} < U_{\rm bare}^{\rm phenanthrene^{3-}}$, and after consideration of the cRPA screening, we obtain $U_{\rm cRPA}^{\rm picene^{3-}} < U_{\rm cRPA}^{\rm coronene^{3-}} \sim U_{\rm cRPA}^{\rm phenanthrene^{3-}}$. Especially in picene^{3-}, the dielectric constant is markedly high ($\sim$12),[63] making the cRPA-U value appreciably small.

We finally remark on some points. As for the C_{60} compounds, the equality $U' \sim U - 2J$ holds among effective parameters. This relationship also roughly holds for the aromatic compounds. The present U values of cRPA for the C_{60} compounds are small compared to the previous estimates of U ($\sim$1–1.5 eV).[35–38] For all materials, the cRPA Coulomb interaction decays as $1/(\epsilon_M^{\rm cRPA} r)$ with r being the distance between the centers of the MLWOs while the fRPA Coulomb interaction is limited to be short ranged due to the metallic screening (see Table VII). We note that the fRPA U gives an opposite trend to the bare and cRPA-U values; for example, in the fcc C_{60} compounds, the fRPA value slightly decreases from fcc-K to fcc-Cs($V_{\rm AFI}$). This is due to the fact that the Coulomb interaction is efficiently screened due to the increase in the density of states accompanied by the decrease of bandwidth. We also found that, in these systems, the exchange interactions J are also efficiently screened; i.e., $J_{\rm cRPA}/J_{\rm bare} \sim 0.3$. This makes a clear contrast to the case of the inorganic materials as $J_{\rm cRPA}/J_{\rm bare} \sim 0.8$ such as the

TABLE VII. U, U', J, and V with three different screening levels [unscreened (bare), constrained RPA (cRPA), and fully screened RPA (fRPA)] for the twelve compounds: fcc-K, fcc-Rb, fcc-Cs($V_{\rm SC}^{\text{opt-}P}$), fcc-Cs($V_{\rm MIT}$), fcc-Cs($V_{\rm AFI}$), A15-Cs($V_{\rm SC}^{\text{high-}P}$), A15-Cs($V_{\rm SC}^{\text{opt-}P}$), A15-Cs($V_{\rm MIT}$), A15-Cs($V_{\rm AFI}$), solid picene^{3-}, solid coronene^{3-}, and solid phenanthrene^{3-}. For the aromatic compounds, two values of U are presented; the left is the lower-level orbital, and the right is the higher-level one. For bare and cRPA U, U', and V values, the units are given in eV, and J is given in meV. For fRPA, the units are given in meV. At the bottom of the table, we present our calculated cRPA-macroscopic-dielectric constant $\epsilon_M^{\rm cRPA}$ in Eq. (11).

	fcc A_3C_{60}					A15 Cs_3C_{60}				Aromatic compounds		
Constant	K	Rb	Cs($V_{\rm SC}^{\text{opt-}P}$)	Cs($V_{\rm MIT}$)	Cs($V_{\rm AFI}$)	$V_{\rm SC}^{\text{high-}P}$	$V_{\rm SC}^{\text{opt-}P}$	$V_{\rm MIT}$	$V_{\rm AFI}$	picene^{3-}	coronene^{3-}	phenanthrene^{3-}
$U_{\rm bare}$	3.27	3.31	3.32	3.35	3.37	3.36	3.39	3.40	3.42	4.43,4.41	4.64,4.59	5.05,5.17
$U'_{\rm bare}$	3.08	3.11	3.12	3.15	3.17	3.16	3.18	3.20	3.22	3.55	4.33	4.55
$J_{\rm bare}$	96	99	100	101	102	97	99	100	101	166	129	275
$V_{\rm bare}$	1.31–1.37	1.30–1.35	1.29–1.34	1.28–1.33	1.27–1.32	1.37–1.38	1.36–1.37	1.35–1.36	1.34–1.34	2.08–2.32	2.79–2.84	2.29–2.43
$U_{\rm cRPA}$	0.82	0.92	0.94	1.02	1.07	0.93	1.02	1.07	1.14	0.73,0.74	1.29,1.26	1.33,1.37
$U'_{\rm cRPA}$	0.76	0.85	0.87	0.94	1.00	0.87	0.95	0.99	1.06	0.58	1.15	1.17
$J_{\rm cRPA}$	31	34	35	35	36	30	36	36	37	53	58	101
$V_{\rm cRPA}$	0.24–0.25	0.26–0.27	0.27–0.28	0.28–0.29	0.30	0.30	0.31	0.32	0.34	0.26	0.59–0.60	0.47–0.48
$U_{\rm fRPA}$	93	91	91	86	83	107	102	99	93	155,151	149,120	166,172
$U'_{\rm fRPA}$	41	39	39	35	32	50	45	42	37	51	53	60
$J_{\rm fRPA}$	25	26	26	26	25	28	28	28	28	38	39	57
$V_{\rm fRPA}$	1–3	1–3	1–3	1–3	1–3	2–3	2	2	1–2	1–4	1–4	2
$\epsilon_M^{\rm cRPA}$	5.6	5.1	4.9	4.6	4.4	4.7	4.4	4.3	4.1	12.0	5.5	6.3

$3d$ transition metals,[39] its oxides $SrVO_3$,[39] and iron-based superconductors.[41,42] As for the alkali-metal intercalation, since it might cause a substantial change in the band structures of the aromatic compounds,[16,17,20] a careful reexamination for the quantitative values of the effective interactions will be desired after the determination of the experimental structures, which remain to be explored.

IV. DISCUSSION

A. Material dependence of effective parameters

Let us move on to a comparison of the effective interaction parameters among the 12 compounds. Figure 6 summarizes the results of the cRPA calculations: the on-site Coulomb repulsion $\bar{U}$ averaged over the MLWOs derived from the target band, the on-site exchange interaction J, the off-site interaction $\bar{V}$ averaged over the nearest-neighbor sites, and the ratio $(\bar{U}-\bar{V})/W$ which measures the correlation strength in the system. Note that the net interaction is estimated as $\bar{U}-\bar{V}$, based on the analysis of the extended Hubbard model.[64]

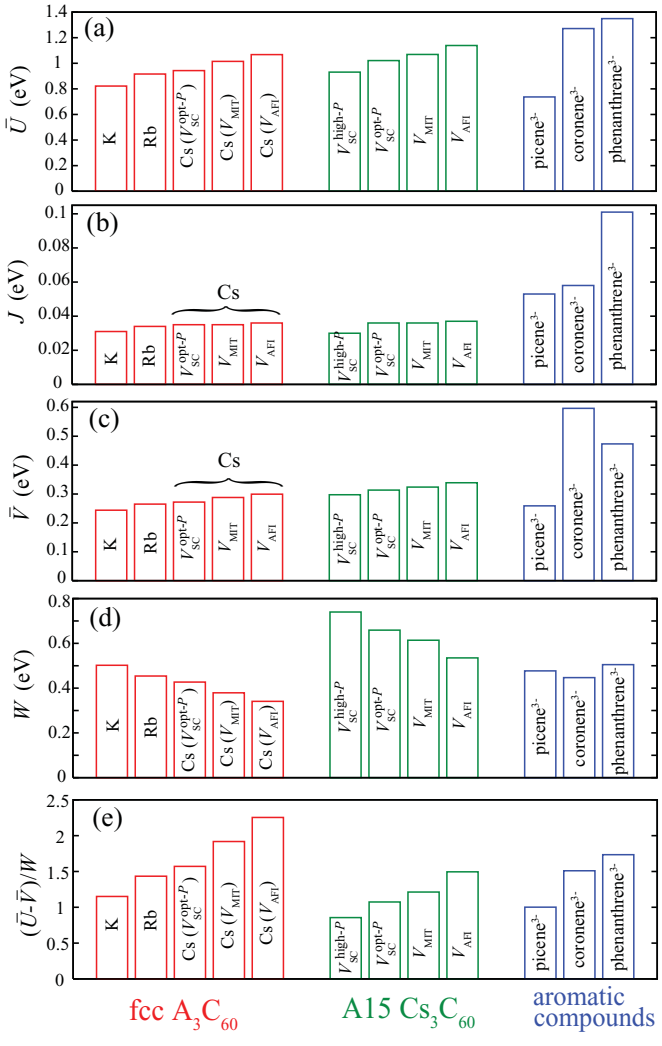

FIG. 6. (Color online) Material dependence of (a) the average of the on-site effective Coulomb repulsion $\bar{U}$, (b) the on-site effective exchange interaction J, (c) the average of the off-site effective Coulomb repulsion between neighboring sites $\bar{V}$, (d) the bandwidth of the target band W, and (e) the correlation strength $(\bar{U}-\bar{V})/W$, which are derived within the cRPA method.

As for the C_{60} systems, we see that $\bar{U}$ has appreciable material dependence, ranging from 0.8 eV to 1.1 eV [Fig. 6(a)]. This is ascribed to the differences in the size of the Wannier orbitals and dielectric screening (see Sec. III E). On the other hand, the material dependence of J is weak, and the value itself is negligibly small as ∼0.03 eV [Fig. 6(b)]. In general, small J favors low-spin states as is observed in experiments.[3–5,65] It is interesting to note that there is a proposal that the Jahn-Teller coupling dominates over the Hund's rule coupling J and induces superconductivity with the help of sufficiently large U.[15] Compared to J, we found that $\bar{V}$ is substantially large as ∼0.3 eV, being as large as ∼25% of $\bar{U}$ [Fig. 6(c)]. As for W, which measures kinetic energy, we observed a decreasing trend as the lattice constant increases [Fig. 6(d)]. We also note that the energy scale for A15 Cs_3C_{60} is larger than that of fcc A_3C_{60} as mentioned in Sec. III B. The derived correlation strength of $(\bar{U}-\bar{V})/W$ exhibits a rather simple monotonic increasing behavior [Fig. 6(e)] with the lattice constant increase. The presented $(\bar{U}-\bar{V})/W \sim 1$ indicates that C_{60} superconductors are categorized as strongly correlated electron systems.

For the aromatic superconductors, we found that the energy scale of $\bar{U}$ is similar to that of the C_{60} superconductors [Fig. 6(a)]. On the other hand, it is interesting to note that the aromatic superconductors tend to have larger J and $\bar{V}$ values [Figs. 6(b) and 6(c)]. We can also see that the material dependence of the interaction parameters among the aromatic superconductors is also more significant since the sizes and shapes of the aromatic molecules are quite different from each other. As for W, they are similar for the aromatic and C_{60} superconductors [Fig. 6(d)]. We found that aromatic superconductors are also in as strongly correlated regimes as the C_{60} ones, based on the analysis of the correlation strength [Fig. 6(e)].

B. Relation between electronic correlation and superconductivity

Next, let us discuss the relation between electronic correlation and superconductivity for the C_{60} and aromatic superconductors. In Figs. 7(a) and 7(b), we plot the superconducting-transition temperature T_c and the Néel temperature T_N as a function of the volume occupied per fulleride anion (V_0) for fcc A_3C_{60} and A15 Cs_3C_{60}, respectively (see also Table I). To see the relation between the electron correlation and the superconductivity, we superimpose a plot of $(\bar{U}-\bar{V})/W$ on the phase diagram. We see that while $(\bar{U}-\bar{V})/W$ and T_c have a positive correlation up to $V_0 \sim 760$–770 Å^3, for larger V_0, electron correlation becomes fatal for superconductivity, and the system eventually becomes an insulator. We note that the critical value of $(\bar{U}-\bar{V})/W$ for the MIT sample is larger for fcc A_3C_{60} (∼1.9) than A15 Cs_3C_{60} (∼1.2). As discussed in Ref. 59, it is important to consider the influence of the lattice and orbital structure on the MIT.[15,66]

In Fig. 7(c), we plot T_c and $(\bar{U}-\bar{V})/W$ for the three aromatic superconductors, which show a negative correlation. Therefore, it seems that electronic correlation does not

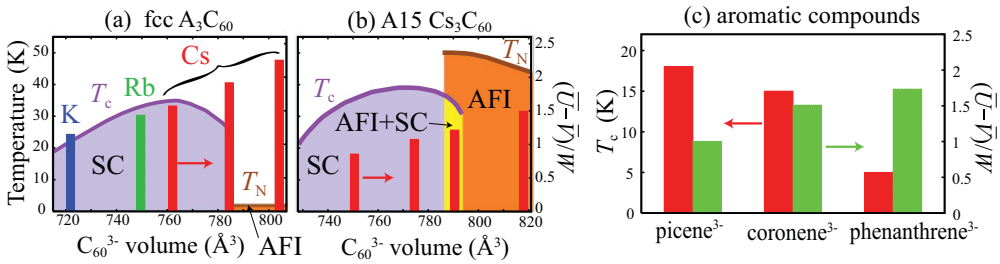

FIG. 7. (Color online) Relations between the experimental curves of the superconducting- and magnetic-transition temperatures (T_c, T_N) as functions of the C_{60}^{3-} volume and the estimated correlation strength $(\bar{U}-\bar{V})/W$ (vertical bar) for (a) fcc A_3C_{60} and (b) A15 Cs_3C_{60}. (c) For aromatic compounds, the measured T_c in Table II and the calculated correlation strength are compared where picene^{3-} = $(C_{22}H_{14})^{3-}$, coronene^{3-} = $(C_{24}H_{12})^{3-}$, and phenanthrene^{3-} = $(C_{14}H_{10})^{3-}$. For the panels (a) and (b), the experimental phase diagrams were taken from Ref. 4 for the fcc and Ref. 3 for the A15 compounds.

favor superconductivity in these aromatic superconductors. Recently, doped 1,2:8,9-dibenzopentacene was found to have a quite high $T_c \sim 33$ K. Since 1,2:8,9-dibenzopentacene is a bigger molecule than picene, coronene, or phenanthrene, the former interaction is expected to be small compared to the latter ones, reflecting the large Wannier spread of the 1,2:8,9-dibenzopentacene molecule. If there is no drastic change in the bandwidth W, which is probable in terms of the tendency shown in Fig. 6(d), the weakest electronic correlation will be realized in doped 1,2:8,9-dibenzopentacene. This trend is consistent with Fig. 7(c).

Regarding the role of the electronic correlation in the C_{60} and aromatic superconductors, there are two possibilities. Either, the pairing mechanism in these compounds has a common root, or these superconductors have completely different pairing glues. If we assume that the aromatic superconductors reside in the vicinity of the border between the superconducting and insulating phases, the first scenario is (at least partially) explicable in relation to the behavior in Fig. 7. On the other hand, in the second scenario, the electronic correlation enhances superconductivity of the C_{60} compounds and inversely suppresses that of the aromatic compounds. In order to clarify this issue, experimental studies to determine the phase diagram for aromatic superconductors against temperature and volume occupied per anion are highly desired.[67] Theoretically, microscopic calculations considering both electronic correlation and electron-lattice coupling are needed, which will be an interesting future problem.

V. SUMMARY

To provide insight into the role of electronic correlation in C_{60} and aromatic superconductors, we derived effective models for a wide range of examples: fcc-K, fcc-Rb, fcc-Cs($V_{SC}^{opt\text{-}P}$), fcc-Cs(V_{MIT}), fcc-Cs(V_{AFI}), A15-Cs($V_{SC}^{high\text{-}P}$), A15-Cs($V_{SC}^{opt\text{-}P}$), A15-Cs(V_{AFI}), solid picene^{3-}, solid coronene^{3-}, and solid phenanthrene^{3-}. To define the basis orbital of the effective model, we constructed MLWOs of isolated bands around the Fermi level. Transfer parameters were derived by evaluating the matrix elements of the Kohn-Sham Hamiltonian between the MLWOs. The low-energy electronic structures of the C_{60} compounds are highly symmetric and isotropic, so the original GGA band is reproduced with only six or seven parameters. On the other hand, the aromatic compounds have quite anisotropic electronic structures.

To quantify the strength of electronic correlation in these compounds, we estimated the effective interaction parameters, such as U, V, and J, by means of the cRPA method. It was found that in addition to the appreciable reduction of the diagonal part of the Coulomb interaction (U and V), the off-diagonal part J is also efficiently screened. Interestingly, all the C_{60} and aromatic superconductors studied in the present work have a similar energy scale for the bandwidth and interaction parameters: $W \sim 0.5$ eV, $U \sim 1$ eV, $J \sim 0.05$ eV, and $V \sim 0.3$ eV. This parameter range suggests that these compounds are a strongly correlated electron system. However, after examination of the material dependence, we found a clear difference between the C_{60} and aromatic compounds in the relation between electronic-correlation strength and T_c; i.e., a positive correlation in the C_{60} system and a negative correlation in the aromatic system.

In the present study, we focused on the derivation for the electronic part of the effective model. For a thorough understanding of the low-energy physics for carbon-based materials, however, the derivation of the electron-phonon interaction part is also imperative. The derivation for this part includes subtle problems concerning the definition of the basis for the phonon mode (see Refs. 68 and 69) and/or the exclusion of the double counting of the screening of the low-energy degree of freedoms, which requires future study.

ACKNOWLEDGMENTS

We thank Taichi Kosugi for providing us with the optimized structure data of undoped coronene and also for stimulating discussions. This work was supported by Grants-in-Aid for Scientific Research (Grants No. 22740215, No. 22104010, No. 23110708, No. 23340095, and No. 19051016). We also acknowledge the Funding Program for World-Leading Innovative R&D on Science and Technology (FIRST program) on "Quantum Science on Strong Correlation," JST-PRESTO, the Strategic Programs for Innovative Research (SPIRE), MEXT, and the Computational Materials Science Initiative (CMSI), Japan.

[1] N. B. Hannay, T. H. Geballe, B. T. Matthias, K. Andres, P. Schmidt, and D. MacNair, Phys. Rev. Lett. **14**, 225 (1965).

[2] A. Y. Ganin, Y. Takabayashi, Y. Z. Khimyak, S. Margadonna, A. Tamai, M. J. Rosseinsky, and K. Prassides, Nat. Mater. **7**, 367 (2008).

[3] Y. Takabayashi, A. Y. Ganin, P. Jeglič, D. Arčon, T. Takano, Y. Iwasa, Y. Ohishi, M. Takata, N. Takeshita, K. Prassides, and M. J. Rosseinsky, Science **323**, 1585 (2009).

[4] A. Y. Ganin, Y. Takabayashi, P. Jeglič, D. Arčon, A. Potočnik, P. J. Baker, Y. Ohishi, M. T. McDonald, M. D. Tzirakis, A. McLennan, G. R. Darling, M. Takata, M. J. Rosseinsky, and K. Prassides, Nature (London) **466**, 221 (2010).

[5] Y. Ihara, H. Alloul, P. Wzietek, D. Pontiroli, M. Mazzani, and M. Riccó, Phys. Rev. Lett. **104**, 256402 (2010).

[6] Y. Ihara, H. Alloul, P. Wzietek, D. Pontiroli, M. Mazzani, and M. Riccó, Europhys. Lett. **94**, 37007 (2011).

[7] R. Mitsuhashi, Y. Suzuki, Y. Yamanari, H. Mitamura, T. Kambe, N. Ikeda, H. Okamoto, A. Fujiwara, M. Yamaji, N. Kawasaki, Y. Maniwa, and Y. Kubozono, Nature (London) **464**, 76 (2010).

[8] X. F. Wang, R. H. Liu, Z. Gui, Y. L. Xie, Y. J. Yan, J. J. Ying, X. G. Luo, and X. H. Chen, Nat. Commun. **2**, 507 (2011).

[9] X. F. Wang, Y. J. Yan, Z. Gui, R. H. Liu, J. J. Ying, X. G. Luo, and X. H. Chen, Phys. Rev. B **84**, 214523 (2011).

[10] Y. Kubozono, H. Mitamura, X. Lee, X. He, Y. Yamanari, Y. Takahashi, Y. Suzuki, Y. Kaji, R. Eguchi, K. Akaike, T. Kambe, H. Okamoto, A. Fujiwara, T. Kato, T. Kosugi, and H. Aoki, Phys. Chem. Chem. Phys. **13**, 16476 (2011).

[11] M. Xue, T. Cao, D. Wang, Y. Wu, H. Yang, X. Dong, J. He, F. Li, and G. F. Chen, e-print arXiv:1111.0820.

[12] For a review, see e.g., O. Gunnarsson, Rev. Mod. Phys. **69**, 575 (1997).

[13] *Handbook of High-Temperature Superconductivity*, edited by J. R. Shrieffer (Springer, New York, 2007).

[14] T. Ishiguro, K. Yamaji, and G. Saito, *Organic Superconductors* (Springer, Heidelberg, 1997).

[15] See M. Capone, M. Fabrizio, C. Castellani, and E. Tosatti, Rev. Mod. Phys. **81**, 943 (2009), and references therein.

[16] T. Kosugi, T. Miyake, S. Ishibashi, R. Arita, and H. Aoki, J. Phys. Soc. Jpn. **78**, 113704 (2009).

[17] T. Kosugi, T. Miyake, S. Ishibashi, R. Arita, and H. Aoki, Phys. Rev. B **84**, 214506 (2011).

[18] P. L. de Andres, A. Guijarro, and J. A. Vergés, Phys. Rev. B **83**, 245113 (2011).

[19] P. L. de Andres, A. Guijarro, and J. A. Vergés, Phys. Rev. B **84**, 144501 (2011).

[20] T. Kosugi, T. Miyake, S. Ishibashi, R. Arita, and H. Aoki, Phys. Rev. B **84**, 020507(R) (2011).

[21] G. Giovannetti and M. Capone, Phys. Rev. B **83**, 134508 (2011).

[22] M. Kim, B. I. Min, G. Lee, H. J. Kwon, Y. M. Rhee, and J. H. Shim, Phys. Rev. B **83**, 214510 (2011).

[23] A. Subedi and L. Boeri, Phys. Rev. B **84**, 020508(R) (2011).

[24] M. Casula, M. Calandra, G. Profeta, and F. Mauri, Phys. Rev. Lett. **107**, 137006 (2011).

[25] F. Roth, M. Gatti, P. Cudazzo, M. Grobosch, B. Mahns, B. Büchner, A. Rubio, and M. Knupfer, New J. Phys. **12**, 103036 (2010).

[26] F. Roth, B. Mahns, B. Büchner, and M. Knupfer, Phys. Rev. B **83**, 165436 (2011).

[27] F. Roth, B. Mahns, B. Büchner, and M. Knupfer, Phys. Rev. B **83**, 144501 (2011).

[28] P. Cudazzo, M. Gatti, F. Roth, B. Mahns, M. Knupfer, and A. Rubio, Phys. Rev. B **84**, 155118 (2011).

[29] While a phonon-mediated mechanism has been proposed,[23,24] the pairing mechanism of superconductivity is still an issue of active debate.

[30] N. Marzari and D. Vanderbilt, Phys. Rev. B **56**, 12847 (1997); I. Souza, N. Marzari, and D. Vanderbilt, *ibid.* **65**, 035109 (2001).

[31] F. Aryasetiawan, M. Imada, A. Georges, G. Kotliar, S. Biermann, and A. I. Lichtenstein, Phys. Rev. B **70**, 195104 (2004).

[32] K. Nakamura, Y. Yoshimoto, T. Kosugi, R. Arita, and M. Imada, J. Phys. Soc. Jpn. **78**, 083710 (2009).

[33] H. Shinaoka, T. Misawa, K. Nakamura, and M. Imada, J. Phys. Soc. Jpn. **81**, 034701 (2012).

[34] K. Nakamura, T. Koretsune, and R. Arita, Phys. Rev. B **80**, 174420 (2009).

[35] R. W. Lof, M. A. van Veenendaal, B. Koopmans, H. T. Jonkman, and G. A. Sawatzky, Phys. Rev. Lett. **68**, 3924 (1992).

[36] M. R. Pederson and A. A. Quong, Phys. Rev. B **46**, 13584 (1992).

[37] V. P. Antropov, O. Gunnarsson, and O. Jepsen, Phys. Rev. B **46**, 13647 (1992).

[38] P. A. Brühwiler, A. J. Maxwell, A. Nilsson, N. Mårtensson, and O. Gunnarsson, Phys. Rev. B **48**, 18296 (1993).

[39] T. Miyake and F. Aryasetiawan, Phys. Rev. B **77**, 085122 (2008).

[40] T. Miyake, F. Aryasetiawan, and M. Imada, Phys. Rev. B **80**, 155134 (2009).

[41] K. Nakamura, R. Arita, and M. Imada, J. Phys. Soc. Jpn. **77**, 093711 (2008).

[42] T. Miyake, K. Nakamura, R. Arita, and M. Imada, J. Phys. Soc. Jpn. **79**, 044705 (2010).

[43] R. Arita, J. Kuneš, A. Kozhevnikov, A. G. Eguiluz, and M. Imada, Phys. Rev. Lett. **108**, 086403 (2012).

[44] P. Hohenberg and W. Kohn, Phys. Rev. **136**, B864 (1964).

[45] W. Kohn and L. J. Sham, Phys. Rev. **140**, A1133 (1965).

[46] When the Hamiltonian is represented in terms of MLWOs, the on-site component of the transfer matrix is not necessarily diagonal, i.e., the basis orbitals which diagonalize this matrix are not always maximally localized. However, it does not cause any problems, as far as we employ the same basis for the one-body and many-body parts of the Hamiltonian. We remark that for the C_{60} compounds, on-site transfers are zero due to the symmetry. For the aromatic compounds, they are found to be 9, 8, and -18 meV for doped picene, coronene, and phenanthrene, respectively.

[47] J. Yamauchi, M. Tsukada, S. Watanabe, and O. Sugino, Phys. Rev. B **54**, 5586 (1996).

[48] J. P. Perdew, K. Burke, and M. Ernzerhof, Phys. Rev. Lett. **77**, 3865 (1996).

[49] N. Troullier and J. L. Martins, Phys. Rev. B **43**, 1993 (1991).

[50] L. Kleinman and D. M. Bylander, Phys. Rev. Lett. **48**, 1425 (1982).

[51] S. G. Louie, S. Froyen, and M. L. Cohen, Phys. Rev. B **26**, 1738 (1982).

[52] O. Zhou and D. E. Cox, J. Phys. Chem. Solids **53**, 1373 (1992).

[53] Initial internal coordinates for optimization are made after Ref. 54 for solid picene and Ref. 56 for solid phenanthrene.

[54] A. De, R. Ghosh, S. Roychowdhury, and P. Roychowdhury, Acta Cryst. C **41**, 907 (1985).

[55] T. Echigo, M. Kimata, and T. Maruoka, Am. Mineral. **92**, 1262 (2007).

[56]J. Trotter, Acta Crystallogr. **16**, 605 (1963).

[57]The volume per C_{60}^{3-} is defined as $V_{\rm conv}/4$ for the fcc structure and $V_{\rm unit}/2$ for the A15 structure with $V_{\rm conv}$ ($V_{\rm unit}$) being the volume of the conventional (unit) cell.

[58]Y. Iwasa, Nature (London) **466**, 191 (2010).

[59]G. R. Darling, A. Y. Ganin, M. J. Rosseinsky, Y. Takabayashi, and K. Prassides, Phys. Rev. Lett. **101**, 136404 (2008).

[60]K. Momma and F. Izumi, J. Appl. Crystallogr. **41**, 653 (2008).

[61]T. Fujiwara, S. Yamamoto, and Y. Ishii, J. Phys. Soc. Jpn. **72**, 777 (2003); Y. Nohara, S. Yamamoto, and T. Fujiwara, Phys. Rev. B **79**, 195110 (2009).

[62]M. S. Hybertsen and S. G. Louie, Phys. Rev. B **34**, 5390 (1986); **35**, 5585 (1987).

[63]We note that the observed large $\epsilon_M^{\rm cRPA}$ of picene^{3-} ($\sim$12) originates from the polarization along the interlayer axis. The value of $\epsilon_M^{\rm cRPA}$ along the interlayer axis is 21.2, and those along the intralayer axis are 6.7 for the $\boldsymbol{a}^*$ axis and 8.2 for the $\boldsymbol{b}^*$ axis. The observed anisotropy is consistent with the result of Ref. 28.

[64]The quantity $(U-V)/W$ is widely employed as a measure for the correlation strength of the effective model. When the quantity is close to or beyond unity, the model is referred to as a strongly correlated system. According to this convention, we measured the correlation strength in the effective models derived for the present 12 materials.

[65]P. Jeglič, D. Arčon, A. Potočnik, A. Y. Ganin, Y. Takabayashi, M. J. Rosseinsky, and K. Prassides, Phys. Rev. B **80**, 195424 (2009).

[66]J. E. Han, E. Koch, and O. Gunnarsson, Phys. Rev. Lett. **84**, 1276 (2000).

[67]Indeed, the measurement of T_c under pressure for alkali- or alkali-earth-metal-doped phenanthrene was performed.[8,9]

[68]W. Kohn, Phys. Rev. B **7**, 2285 (1973).

[69]F. Giustino, M. L. Cohen, and S. G. Louie, Phys. Rev. B **76**, 165108 (2007).